Lattice-embedded Ni single-atom catalyst on porous Al_2O_3 nanosheets derived from Ni-doped carbon dots for efficient propane dehydrogenation

Rui Ma [a,*], David P. Dean [b], Junxian Gao [b], Mingshan Wang [a], Yuan Liu [a,*], Kaijun Liang [a], Junbo Wang [a], Jeffrey T. Miller [b], Bo Zhou [a,*], Guojun Zou [a], Jiajing Kou [c,*]

[a] Guangdong Laboratory of Chemistry and Chemical Engineering, Shantou 515031, China
[b] Davidson School of Chemical Engineering, Purdue University, 480 Stadium Mall Drive, West Lafayette, IN 47907, United States
[c] School of Vehicles and Energy, Yanshan University, Qinhuangdao 066000, China

ARTICLE INFO

ABSTRACT

The controlled synthesis of highly durable single-atom catalysts (SACs) for high-temperature applications remains a great challenge. Herein, we develop a facile strategy to construct Al_2O_3 lattice-embedded Ni SAC via thermal treatment of aluminum oxide encapsulated Ni-doped carbon dots (Ni-CDs@Al_2O_3). Detailed studies reveal that the Ni atoms are released from carbon matrix and simultaneously captured by cation defects formed in situ within a phase transformation of aluminum oxide. Al_2O_3 stabilized Ni atoms via Ni-O_4 coordination are well illustrated by combined characterizations. For propane dehydrogenation, reactivity measurements show that the center of Ni-O ion pairs effectively activates C_3H_8 and the higher rate of C_3H_6 formation on Ni SAs than Ni NPs, by a factor of 12, is the result of inhibition of C-C bond cleavage involving side reactions, as identified by density functional calculations. Beyond that, this lattice-embedded Ni SAC exhibits superior stability and recyclability in long-term operation with little coke accumulation.

1. Introduction

Single-atom catalysts (SACs) is an emerging material system in heterogeneous catalysis that offers benefits to chemical reactions with near 100% atom utilization and tunable catalytic properties [1–3], showing potential for next-generation industrial catalysts. However, the controllable synthesis of SACs with desired catalytic stability and recyclability remains challenging because of the strong tendency of migration and aggregation of metal atoms in high-temperature applications [4], e.g. catalytic dehydrogenation of light alkanes. Non-oxidative propane dehydrogenation (PDH) is an industrial method for on-purpose production of valuable propylene and hydrogen [5]. Normally, high operation temperatures (>550 °C) are required to obtain considerable per-pass propylene yield in this endothermic process [6]. Alumina supported Pt-Sn bimetallic and CrO_x oxide catalysts have been applied in commercial PDH processes [5,6]. Yet, the application of Pt-based catalyst is strongly limited by its high expense and cumbersome regeneration steps, while CrO_x-based catalyst suffers from environmental issues [7]. The development and understanding of alternative PDH catalyst is thus an intense field of research.

Previous studies have proposed that the atomic configurations of active center have a significant impact on the product distribution during propane conversion [8–10]. Typically, the site of multiatom ensembles are favored by side reactions involving C-C (H) scissions, including cracking and deep dehydrogenation, where multipoint contact of molecule and metal atoms are required to complete the reaction path [11,12]. This leads to the production of methane and coke. Correspondingly, these undesired reactions are largely suppressed by decreasing the size of metal nanoparticle (NP) or alloying with an inert metal [13–15], whereas parallel dehydrogenation process is less suppressed due to the single-atom-adsorbed intermediate for dehydrogenation of propane [16]. To this end, the unique geometric structure of SACs is appealing for effective conversion of propane while suppressing undesired side reactions.

For SACs synthesis, metal atoms are usually anchored on the appropriate transition metal oxides by bonding between metal atoms and donor atoms from the support (e.g. oxos) to construct M-O_x moieties (x = 2 ~ 4) [17–21]. In general, such metal oxides often have a less hierarchical porous structure with comparison to the zeolite-based materials, and the aggregation of metal atoms is inevitable during frequent

---

reaction-regeneration cycles. Therefore, fabricating of thermally stable SACs necessitates the formation of strong bonds between metal atoms and the underlying support. Lattice-embedded metal atoms in non-reducible oxides or zeolites have been developed as an effective strategy to prevent metal atoms from being usurped from the M-O$_x$ moieties [22,23], even in the presence of hydrogen at elevated temperatures. For instance, the siliceous zeolite frameworks stabilized isolated Fe$^{\delta+}$ sites by Si-O-Fe$^{\delta+}$ linkage [24] and the substitution of Mg by Ni atoms in the MgO lattice (Ni$_x$Mg$_{1-x}$O) [25] were reported to possess stable performance in high-temperETURE applications (>500 °C). Alumina is a support of choice for industrial PDH catalysts, and is thus used to construct lattice-embedded SACs due to its good thermal stability and diverse defects in its lattice matrix [26]. Work by Li et al. [27] prepared the noble metal SACs using cation defects in AlCo$_2$O$_4$ as the atoms capturing site, and the resulting Pd SAC possesses extraordinary (hydro)thermal stability for CO and propane oxidation. Nevertheless, it remains unclear how well these sites would survive from highly reductive reaction conditions. The combustion of platinum acetylacetonate and zirconium butoxide in a flame spray pyrolysis process was reported to be an effective strategy for substitution of support cation by Pt cation, generating the lattice-embedded Pt SACs [28]. Inspired by this, heat treatment of appropriate metal and alumina precursors is likely to induce the strong interaction between metal atoms and alumina.

Nickel-based catalysts have been shown to be particularly effective for activation of alkane molecules [29,30]. However, deep dehydrogenation of generated propylene is more favorable than propylene desorption on the metal Ni surface, through density functional theory (DFT) calculations [31,32], decreasing the olefin selectivity and catalyst life. Our previous studies [33,34] on atomically dispersed Ni catalysts for PDH have demonstrated the significant inhibition of the C-C bond cleavage on the site of isolated Ni atoms, thus improve propylene selectivity. However, the intrinsic activity and catalytic stability of reported Ni-based catalysts are not satisfactory compared with that of Pt-based catalysts, providing opportunity for fine regulation of Ni sites for efficient conversion of propane. Herein, we report the successful fabrication of the Ni SAC with Ni atoms embedded in the Al$_2$O$_3$ lattice derived from Ni-doped carbon dots (Ni-CDs). The controllable synthesis of Ni-CDs is critical to achieve the substitution of Al cations by Ni atoms in the Al$_2$O$_3$ lattice and the formation of abundant mesoporous channels on Al$_2$O$_3$ sheets, through detailed characterizations, the formation mechanism of lattice-embedded Ni SAC has been revealed. The lattice-embedded Ni single-atom sites via Ni-O$_4$ coordination possess excellent catalytic stability and improved C$_3$H$_6$ formation rate for PDH, with no significant deactivation and little coke accumulation within several reaction-regeneration cycles. Kinetic measurements and DFT calculations were performed to validate the enhancement of the sintering-resistant Ni SAC. This study on alumina-supported SAC paves a way for the rational design and synthesis of high-efficient SACs for H$_2$-involved high temperature applications.

2. Materials and methods

2.1. Chemicals

The analytical reagents of ethanediamine (EDA, >99%), citric acid monohydrate (CA, 98%), and nickel nitrate hexahydrate (>98%), as well as nitric acid (65–68%) were obtained from Shanghai Macklin Biochemical Co., Ltd. (Shanghai, China). Commercial-grade boehmite powder (Qingdao Haiyang Chemical Co. Ltd., China) was purchased to prepare alumina-supported nickel catalysts. All chemicals were directly used as received without further purification.

2.2. Catalyst preparation

The Al$_2$O$_3$ nanosheets stabilized Ni single atoms, named Ni SAs/N-Al$_2$O$_3$ (where N meaning nanosheet), was prepared using a two-step process, consisting of hydrothermal synthesis of Ni-CDs and the subsequent loading of Ni species via thermal treatments of the composite of Ni-CDs@Al$_2$O$_3$. First, a peptized form of boehmite was prepared by adding 10 g boehmite powder to 100 mL of a dilute HNO$_3$ solution (0.15 M) under vigorous stirring. The suspension was then sealed and kept at 60 °C in an oil bath. After continuous stirring for 24 h, a transparent alumina sol was obtained. In a typical hydrothermal synthesis of Ni-CDs, CA (1.1 g) and Ni^{2+} salt (0.5 g) were first dissolved in 40 mL of deionized water while stirring. Next, a required amount of EDA was added to the Ni^{2+} solution dropwise, and immediately a clear blue solution was formed. After stirring for another 0.5 h, the resulting solution was transferred into a Teflon-lined stainless steel autoclave and stored in a 150–180 °C oven for 3–5 h, followed by cooling to room temperature. The solution of Ni-CDs was dialyzed through a dialysis tube (1000 Da) for 2 days to remove the remaining salts and small fragments. A stoichiometric amount of Ni-CDs (1 wt% of Ni loading, compared with Al$_2$O$_3$ to be generated) was added dropwise into the alumina sol while stirring. After continuous stirring for 2 h at room temperature, the suspension was heated to 70 °C for water evaporation until the sol became a slurry. Afterward, the resulting slurry was dried at 90 °C overnight, followed by calcining in static air at 600 °C for 4 h and treating in flowing 10% H$_2$/Ar (50 mL/min) at 600 °C for 2 h, obtaining Ni SAs/N-Al$_2$O$_3$ sample. As a comparison, an alumina supported Ni NPs catalyst was prepared by the same dry and thermal treatments of the mixture of Ni^{2+} and alumina sol, and the obtained sample is denoted as Ni NPs/Al$_2$O$_3$.

2.3. Characterization

The catalyst nickel loadings were determined by a PerkinElmer ICP 2100. The textural properties of alumina-supported Ni catalysts were characterized by means of N$_2$ adsorption-desorption experiments (Micromeritics ASAP2020), and the samples were degassed at 300 °C for 6 h to eliminate physically adsorbed compounds before data collecting. Temperature programmed hydrogen-reduction (H$_2$-TPR) was performed using a chemisorption instrument (Micrometric ChemiSorb 2750). Powder X-ray diffraction (XRD) patterns were recorded on a Bruker D8 diffractometer using Cu Kα as a radiation source with a scan rate of 2° per min. X-ray photoelectron spectroscopy (XPS) experiments were conducted on a K-Alpha spectrometer (Thermo Scientific) equipped with an Al Kα anode, and the binding energy of C 1 s peak (B.E. = 284.6 eV) was set as the calibration of Ni. Thermogravimetric (TG) and differential scanning calorimetry (DSC) analysis of the samples were carried out on Mettler Toledo instrument (TGA/DSC 3 +) in flowing 20% O$_2$/N$_2$ at a heating rate of 10 °C/min up to 800 °C. The experiments were performed on as-dried samples before their calcination.

The morphology and the structure of as-prepared Ni-CDs and the alumina-supported Ni catalysts were visualized by scanning electron microscopy (SEM, Verios 5UC), transmission electron microscopy (TEM, Talos F200), and high-angle annular dark-field scanning transmission electron microscopy (HAADF-STEM, Titan Cubed Themis G2 300). X-ray absorption spectroscopy (XAS) experiments of alumina-supported Ni samples were conducted at the 10-BM beamline at the Argonne National Laboratory (ANL) Advanced Photon Source (APS). The scans were taken in transmission mode at the Ni K-edge using three consecutive ion chambers to enable simultaneous measurement of the sample as well as a Ni foil energy reference. Each sample was ground and pressed into a wafer inside a stainless-steel sample holder with six apertures which allows for identical simultaneous gas and temperature treatment. The sample holder was loaded into a quartz tube reactor with gas lines attached and placed inside a clamshell furnace. The quartz tube has X-ray transparent windows on each end for transmission mode scanning. There were three pre-treatment conditions applied to each sample, including under air, diluted H$_2$, and C$_3$H$_8$ atmosphere respectively in the temperature range of 580–600 °C. All samples were pre-treated at high temperature, but were cooled to room temperature and scanned in He.

XAS data were processed using WinXAS software [35]. Simulated phase and amplitude functions for Ni-O, Ni-Al, and Ni-Ni scattering were extracted using Feff6 [36]. The extracted *chi* was k^2-weighted and Fourier transformed over a *k* range of 2.5 to 10 Å^{-1} for the samples. The S_0^2 value was determined by fitting the NiO reference compound. Fitting was performed in *q*-space to determine the Debye-Waller factor, σ^2.

2.4. Catalytic evaluation

The reaction tests of PDH were performed in a fixed-bed quartz micro-reactor (6 mm inner diameter) under atmospheric pressure using 0.1–0.3 g of catalyst (40–60 mesh) mixed with quartz sand (40 mesh) was loaded to give a constant total volume (0.5 mL) for each test sample. The test temperatures were controlled by a cylindrical furnace, and a K-type thermocouple was inserted directly above the catalyst bed inside the quartz tube to ensure accurate temperature record. Prior to the catalytic measurements, the sample was heated to test temperature under 50 mL/min N_2 flow (99.99%) and held at this temperature for 0.5 h. The flow rate of input gas was metered into the reactor by means of digital mass flow controllers (Bruker), which were pre-calibrated by a bubble flow meter. Following the pretreatment, the sample was exposed to flowing mixtures of C_3H_8/N_2 prepared by diluting pure C_3H_8 (99.98%) stream with N_2 (99.999%) to give 20% of C_3H_8. Gas flow rates of the C_3H_8/N_2 were varied (10–90 mL/min) to obtain space time (defined as $g_{Cat}\cdot h/mol_{C3H8}$) ranging from 0.05–0.5 $g_{Cat}\cdot h/mol_{C3H8}$. For each test temperature investigated, rate measurements were recorded at four different space times, and the effect of the secondary reactions and product inhibition on the reaction kinetics was eliminated by extrapolating linearly to zero space time. The reaction products in outlet gas, including C_3H_6, C_2H_4, C_2H_6, and CH_4, were detected and quantified using an online gas chromatography (Agilent 8890) equipped with an FID detector. The carbon balance of the samples during C_3H_8 was calculated basing on the mass balance between introduced and produced carbons. The conversion of C_3H_8 and C_3H_6 selectivity were defined as follows:

$$\text{Conv}(\%) = \frac{\text{moles of propane in inlet} - \text{moles of propane in outlet}}{\text{moles of propane in inlet}} \times 100\%$$

(1)

$$\text{Sel}\quad(\%) = \frac{\text{moles of propylene}}{\text{moles of propylene} + \frac{2\times\text{moles of C2}}{3} + \frac{\text{moles of methane}}{3}} \times 100\%$$

(2)

The catalyst stability test was performed at 580 °C, and 0.3 g of Ni SAs/N-Al$_2$O$_3$ and 20 mL/min of 20% C_3H_8 balanced with N_2 were used. After each 24 h PDH reaction, the Ni SAs/N-Al$_2$O$_3$ was regenerated by feeding 50 mL/min of dry synthetic air (20% O_2 balanced with N_2) and held for 0.5 h. The gas flow was then switched to 100 mL/min of flowing N_2 for next PDH run. The deactivation rate (k_d) within 24 h reaction was determined using the Eq. (3), where $Conv_0$ and $Conv_t$, respectively are the initial and final C_3H_8 conversions [37,38]. The turnover frequency (TOF) of the Ni-based catalysts is expressed as the mole of converted propane per mole of active atoms per second. The nickel dispersion of Ni NPs/Al$_2$O$_3$ is determined based on the average size of Ni NPs while assuming nickel dispersion of Ni SAs/N-Al$_2$O$_3$ is 100% [39]. The values of apparent activation energy (*E*a) over alumina-supported Ni catalysts were determined by Arrhenius plots, and low C_3H_8 conversions (<10%) were recorded by adjusting the temperature ranging from 520 to 600 °C.

$$k_d = \frac{\ln\left(\frac{1-\text{Conv}_t}{\text{Conv}_t}\right) - \ln\left(\frac{1-\text{Conv}_0}{\text{Conv}_0}\right)}{t}$$

(3)

2.5. Computing method

Calculations of energy profiles for reaction mechanism were based on generalized gradient approximation (GGA) of Perdew-Burke-Ernzerhof (PBE) functional [40] with the projector augmented wave (PAW) pseudopotentials [41] and a plane-wave cutoff energy of 400 eV in VASP [42,43]. A Gamma centered Monkhorst Pack type special *k*-point grid [44] $2 \times 2 \times 1$ was used for Brillouin Zone (BZ) integration. Atomic positions were optimized until the forces were less than 0.02 and 0.05 eV/Å for the intermediate structures and transition state structures, respectively. Transition states were searched by climbing image nudged elastic-band method (CI-NEB) [45] and further confirmed by vibrational frequency analysis. Free energy correction was performed at 853.15 K with details shown in the supporting information (SI).

The structure model of active center on Ni SAs/N-Al$_2$O$_3$ was built on the γ type Al$_2$O$_3$ (100) surface by replacing one Al atom with one Ni atom. The convergence test of the vacuum for the DFT calculation was conducted, as shown in Fig. S1, and a 10 Å vacuum space was used to separate the slabs. The cell parameters are a= 11.174 Å, b= 8.413 Å, c= 16.438 Å. The atoms at the bottom layer were fixed and those at the top layer were relaxed in the simulation.

3. Result and discussion

3.1. Preparation and characterizations of Ni SAs/N-Al$_2$O$_3$

A model of the synthesis process used to achieve atomically dispersed Ni atoms on porous alumina sheets is presented in Fig. 1a. In this preparation of SACs, the key is the controllable synthesis of Ni-CDs, which is prepared via a one-pot hydrothermal method using CA and EDA as carbon source and surface passivation reagent, respectively. These small molecules (Ni^{2+}, CA, and EDA) possess amine, carboxyl, and hydroxyl groups which first react with each other by chelation, polycondensation and inner cyclization to form small crosslinked polymer clusters, as pictured in Fig. S2. These species are then carbonized at elevated temperatures, resulting in the formation of Ni-CDs. The influence of synthesis conditions, including hydrothermal temperature, reaction time, and the ratio of EDA to CA, on the morphology and size of obtained hybrid materials are discussed through TEM analysis, as illustrated in SI (Figs. S3–5). In summary, raising hydrothermal temperature and/or prolonging reaction time increase the degree of dehydration and further carbonization processes, leading to the formation of uniform particle size of CDs with higher carbonization degree. Beyond that, we have noted that decreasing the ratio of EDA to CA tends to obtain CDs with a larger particle size. The optimal synthesis conditions for the Ni-CDs were determined as 180 °C for 5 h with a molar composition of Ni^{2+}: CA: EDA = 1: 3: 6. As-prepared Ni-CDs were then used to synthesize Ni SAs/N-Al$_2$O$_3$.

TEM images in Fig. 1b-d show the uniform dispersion of Ni-CDs without apparent aggregation, and the spherically-shaped particles are mainly in the size range from 2 to 3 nm, giving an average size of 2.1 nm. From the high-resolution TEM image (Fig. 1c), most particles exhibit well-resolved lattice fringes, with a lattice spacing of 0.21 nm referring to the (100) facet of graphite carbon [46]. The previous XAS studies [47,48] on metal-doped CDs obtained by a similar hydrothermal method have demonstrated that the metal atoms chelate with the carbon matrix mainly through M-C and M-N bonding, and no particles of metal atoms were detected by EXAFS analysis. Namely, the metal species are confined in well-structured CDs in the form of isolated metal atoms. Moreover, the EDS mapping image of Ni-CDs (Fig. 1d) is indicative of uniformly dispersed Ni atoms in the CDs.

During the calcination of Ni-CDs@Al$_2$O$_3$ composite, the violent atom migration relating to the pyrolysis/oxidation of carbon species and the dehydration of alumina precursor led to the redispersion of Ni atoms, and such process was demonstrated by TG/DSC analysis (Fig. 1e). The thermogravimetric plot of the boehmite shows two main mass loss events with maximum loss rate at 59 and 422 °C, respectively, which agree with the two endothermic peaks in the DSC curve (Fig. S6a). These two mass loss events are attributed to the departure of water molecules from the boehmite at different stages, leading to the generation of
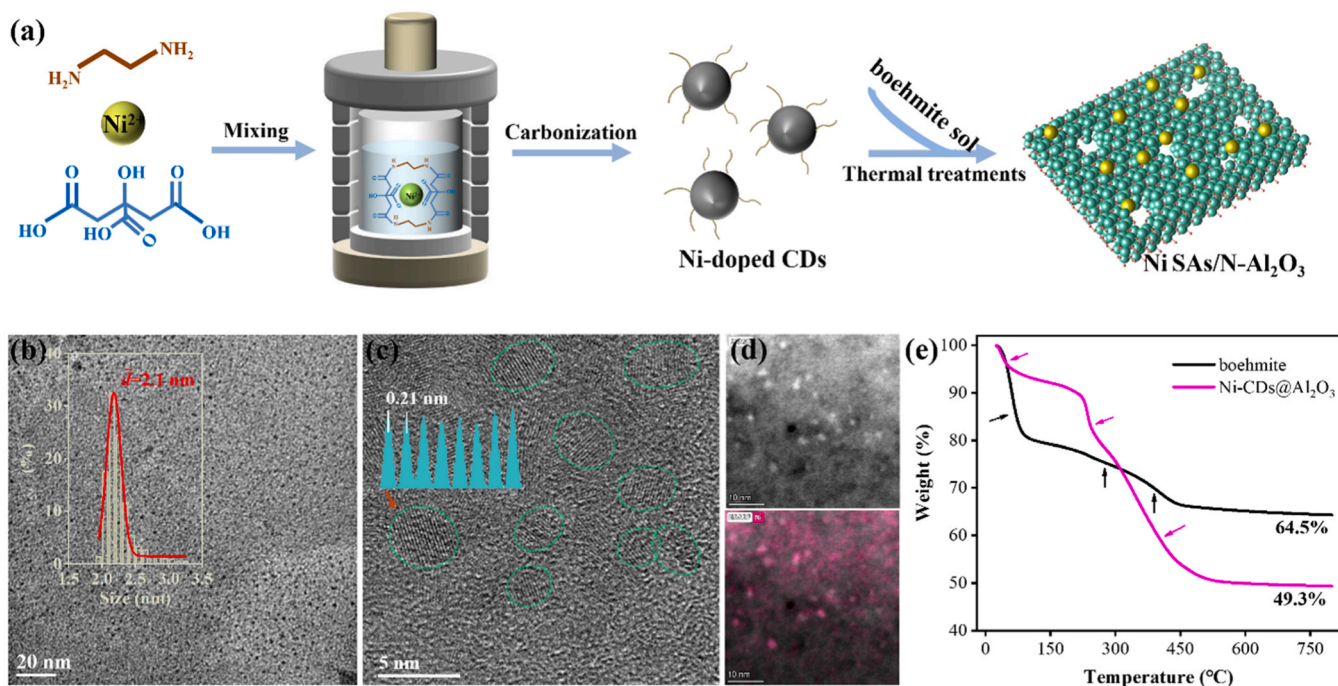
Fig. 1. (a) Schematic illustration of synthesis process of Ni SAs/N-Al_2O_3 catalyst. (b) TEM image and corresponding particle size distribution of Ni-CDs. (c) HRTEM image of Ni-CDs. The particle outlines are marked with dotted green circles. (d) STEM image and corresponding EDX Ni map of Ni-CDs. (e) TG curves of as-dried boehmite powder and Ni-CDs@Al_2O_3 composite.
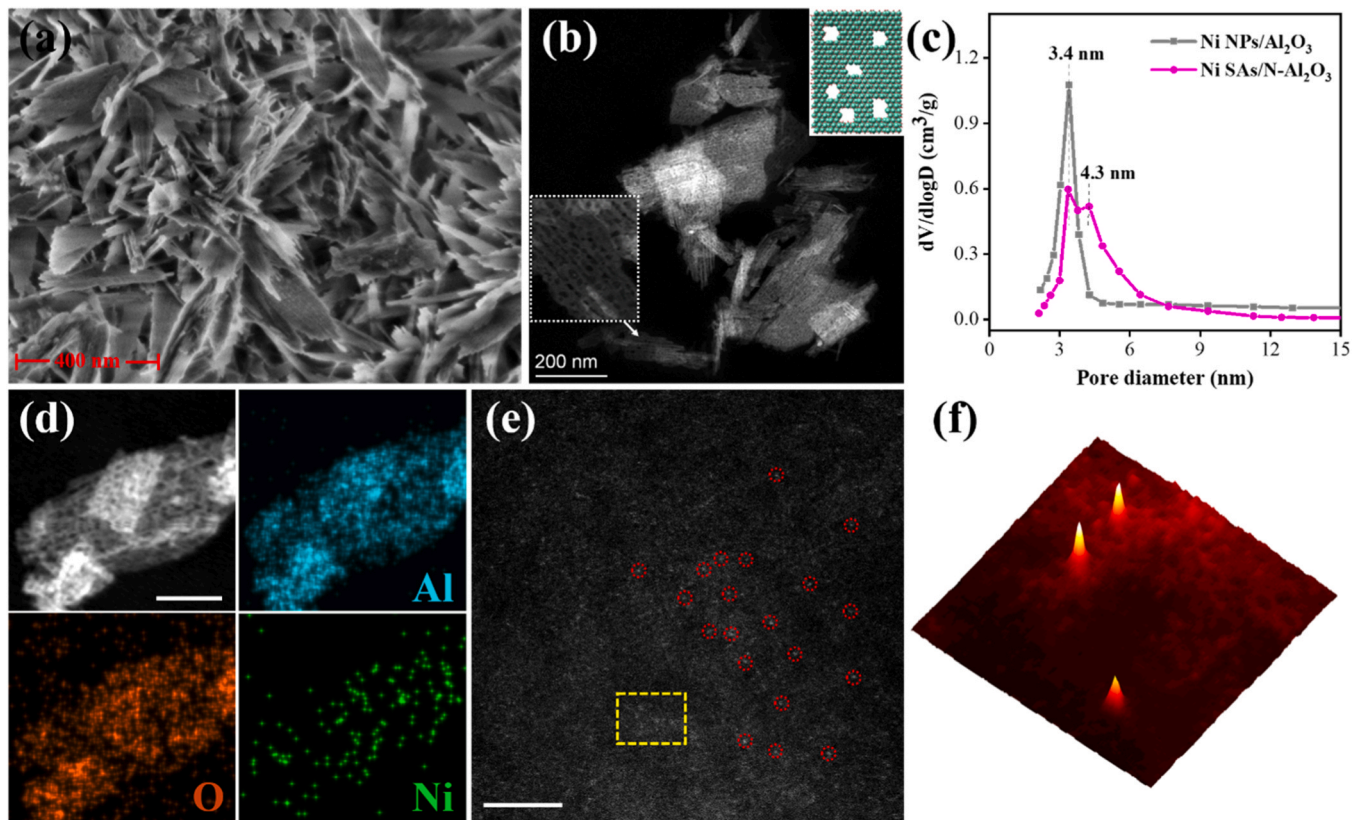

Fig. 2. (a, b) SEM and TEM images of the Ni SAs/N-Al_2O_3. The inset is the magnified region of TEM with a schematic model for the mesoporous Al_2O_3. (c) Pore size distribution curves for the alumina-supported Ni catalysts. (d) HAADF-STEM image and STEM-EDS elemental mapping images of Ni SAs/N-Al_2O_3. Scale bar, 20 nm. (e) C_s-corrected STEM image of the Ni SAs/N-Al_2O_3. Scale bar, 2 nm (f) Atom-overlapping Gaussian function fitting mapping of the yellow rectangle in panel (e).

γ-Al$_2$O$_3$. Specifically, first endothermic peak at 59 °C is ascribed to dehydration of physisorbed water molecules, while second endothermic peak at 422 °C suggests further dehydration from crystalline structure of Al oxide. Based on the weight loss between 100 and 800 °C (16.5%), we obtain the formula of the starting boehmite to be AlOOH·0.6 H$_2$O, which agrees with previously reported data (0.45–0.8) [49]. The weight loss at high temperature has been attributed to molecules chemisorbed on Al^{3+} and O^{2-} sites localized on the (100) and (001) faces [50]. Namely, there are an abundant defect sites on the metastable state of alumina, serving as anchoring sites for bonding heteroatoms. As can be seen from Fig. S6b, TG/DSC curves of Ni NPs/Al$_2$O$_3$ precursor show two endothermic peaks (53 and 408 °C) and almost the same total mass loss as boehmite, suggesting that the addition of small amounts of nickel nitrate has little effect on the structural transformation of boehmite during calcination. By contrast, the TG/DSC curves of Ni SAs/N-Al$_2$O$_3$ precursor reveal significantly different characteristics of weight loss and corresponding thermal effects. For the Ni-CDs@Al$_2$O$_3$ composite, no obvious endothermic peaks in the temperature range of 100–600 °C are observed in DSC curve. Instead, two sharp exothermic peaks (236 and 340 °C) are observed, resulting from the combustion of carbon species. The total weight loss of Ni SAs/N-Al$_2$O$_3$ precursor is over 50%, and the ~15% more weight loss compared to boehmite sample can be attributed to the content of CDs. The structural transformation from boehmite to γ-Al$_2$O$_3$ after calcination is also confirmed by XRD spectra shown in Fig. S7, and the absence of diffraction signals of nickel species on both alumina-supported Ni catalysts indicates the high dispersion of Ni on γ-Al$_2$O$_3$.

The ICP-MS analysis shows agreement between the calculated and real nickel loadings (1.1 wt% for Ni SAs/N-Al$_2$O$_3$ and 1.0 wt% for Ni NPs/Al$_2$O$_3$). Fig. 2a presents an SEM image of Ni SAs/N-Al$_2$O$_3$, and the flowerlike aggregate looks like construction of numerous alumina nanosheets. The morphologies of alumina are further characterized by TEM, as displayed in Fig. 2b and Fig. S8, and porous alumina nanosheets with a thickness of about 18 nm can be clearly observed. From the inserted TEM image at a high magnification, the yielded channels with the diameter range of 3–5 nm are situated uniformly across the alumina laminates. However, such pores cannot be found on the sample of Ni NPs/Al$_2$O$_3$ (Fig. S9). Therefore, the CDs also serve as pore-forming additive to produce a new pore structure during the calcination process. N$_2$ adsorption-desorption measurements were performed to reveal the different pore characteristics of γ-Al$_2$O$_3$ with/without addition of CDs. As can be seen from Fig. S10, both samples show type IV isotherms with H1 hysteresis loops characteristic of mesoporous materials, attributing to cylindrical mesopore channels [51]. Differing from the N$_2$ adsorption-desorption isotherm of Ni NPs/Al$_2$O$_3$, the condensation step for Ni SAs/N-Al$_2$O$_3$ is slightly shifted to greater relative pressure, with a decrease in the steepness of the capillary condensation step, which corresponds with the presence of larger irregular mesopores [52]. Fig. 2c shows the BJH size distribution curves of the alumina-supported Ni samples. The Ni NPs/Al$_2$O$_3$ exhibits a surface area of 142 m^2/g with a mean pore size of 3.5 nm. However, for sample Ni SAs/N-Al$_2$O$_3$, there is a clear bimodal pore size distribution with one peak around 3.4 nm and another broader peak around 4.3 nm. When CDs combust, additional pores are created with different sizes depending on the particle size and content of as-prepared CDs. Compared with Ni NPs/Al$_2$O$_3$, Ni SAs/-N-Al$_2$O$_3$ exhibits a higher BET surface area (236 m^2/g) and developed porosity, suggesting that the size-adjustable CDs can be used as an effective pore-forming agent for improving the textural properties of mesoporous γ-Al$_2$O$_3$. The EDX elemental intensity maps of Ni SAs/-N-Al$_2$O$_3$ show the prevalence of Ni to be distributed uniformly. From HAADF-STEM image (Fig. 2e), Ni single atoms can be identified as isolated bright dots which have been indicated within the dotted red circles. A three-dimensional isolines (Fig. 2 f) of the yellow rectangle in Fig. 2e further reveals the heavier Ni atoms decorated on the surface of mesoporous γ-Al$_2$O$_3$ substrate. By contrast, the formation of NPs with a clear crystalline structure of metallic Ni is observed in the TEM image of

Ni NPs/Al$_2$O$_3$ catalyst, and the average size of the Ni NPs is 3.9 nm (Fig. S11a). Additionally, Cs-corrected STEM image and corresponding three-dimensional isolines of Ni nanoparticle over Ni NPs/Al$_2$O$_3$ further demonstrates the absence of atomically dispersed Ni species around Ni nanoparticle (Fig. S11b-c), suggesting the aggregated Ni NPs were generated on Ni NPs/Al$_2$O$_3$ after reduction process.

XAS experiments were performed to acquire more information about the atomic coordination and structural signature of nickel sites in Ni SAs/N-Al$_2$O$_3$. Fig. 3a shows the spectra of X-ray absorption near edge structure (XANES), which displays the qualitative similarity of Ni SAs/N-Al$_2$O$_3$ sample to the NiO reference, supporting the formation of Ni^{2+} species. The oxidation state of nickel is also confirmed by XPS and H$_2$-TPR analysis (Fig. S12 and Fig. S13). The pre-edge peak in the enlarged spectra corresponds with a dipole-forbidden but quadropole-allowed transition (1 $s{\rightarrow}3d$) [53]. The pre-edge feature of Ni SAs/N-Al$_2$O$_3$, compared with the NiO reference (8342.7 eV), shifts to lower energy (8340.6 eV), which is indicative of the transform from octahedral to tetrahedra Ni-O coordination [34]. This may be due to the strong interaction between the Ni species and the γ-Al$_2$O$_3$ support, which is evidenced by the shorter Ni-O bond distance (2.03 Å) in the sample relative to the NiO reference (2.08 Å), as shown in the spectra of X-ray absorption fine structure (EXAFS) in Fig. 3b. The representative fits and fitting parameters for Ni SAs/N-Al$_2$O$_3$ are presented in Fig. S14 and Table S1. The real and imaginary portions of the Fourier-transform magnitude of Ni SAs/N-Al$_2$O$_3$ and NiO are plotted in Fig. S14d, showing a fundamentally different bond distance for both the first and second shells. For Ni SAs/N-Al$_2$O$_3$, fitting results show a Ni-O coordination of 4.1 at a bond distance of 2.03 Å, suggesting the tetrahedral coordination aligns with the structure of ionic Ni sites on alumina. The EXAFS in R space for the Ni SAs/N-Al$_2$O$_3$ catalyst regardless of treatment in H$_2$ at 600 °C or C$_3$H$_8$ at 580 °C are qualitatively identical, as shown in Fig. S15, suggesting the extraordinary thermal stability and anti-reduction capacity of Ni^{2+}-O$_4$ moieties. EXAFS fitting was also conducted on the second shell (peak located above 2 Å), and the fitting results are given in Table S2. For the NiO reference, the bond distance for the first shell Ni-O is 2.08 Å with a coordination of 6 and the bond distance for second shell Ni-O-Ni is 2.94 Å with a coordination of 12. By fitting the second shell peak of Ni SAs/N-Al$_2$O$_3$ with either a Ni-O-Ni or Ni-O-Al scatting path, the second shell Ni-O-Ni scattering path yields a non-realistic result with an E$_0$ shift of − 13.0 eV at a longer bond distance of 2.94 Å. Using a Ni-O-Al scattering path, we report a realistic fit with a low least squares regression value as pictured in Fig. S14c along with a reasonable E$_0$ shift of 3.8 eV at a shorter bond distance of 2.88 Å. Thus, the second shell can be attributed to Ni-O-Al scattering.

The above results confirm that the Ni-embedded in the γ-Al$_2$O$_3$ lattice is routinely achievable. On the Ni SAs/N-Al$_2$O$_3$ sample, Ni atoms are atomically bonded with four oxygen atoms from crystalline Al oxide, yielding a formal oxidation state of + 2. During the thermal treatment of Ni-CDs@Al$_2$O$_3$, the change of coordination structures of Ni atoms occurs, and the formation of Ni-O-Al bonding suggests the substitution of Al atoms by Ni atoms in the crystalline structure of γ-Al$_2$O$_3$. The single atom Ni sites exhibit superior thermal stability and maintain their single-atom tetrahedrally-coordinated nature regardless of high temperature treatments in hydrogen or propane. Moreover, the sacrifice of carbon dots during calcination lead to the formation of dense channels on alumina sheets, which undoubtedly expose more lattice-embedded Ni sites for catalytic reactions.

3.2. PDH test

We then measured the kinetics of propane conversion over alumina-supported Ni catalysts. Fig. 4a exhibits a stable rate for C$_3$H$_8$ conversion (~ 6.2 mmol$_{C3H8}$·g$_{Cat}^{-1}$·h^{-1}) and good carbon balances (>98.5%) during the 100 min time on stream (TOS) over Ni SAs/N-Al$_2$O$_3$ catalyst. Notably, the rate of C$_3$H$_8$ conversion over Ni NPs/Al$_2$O$_3$ decreases monotonically during the first 20 min of reaction. According to our
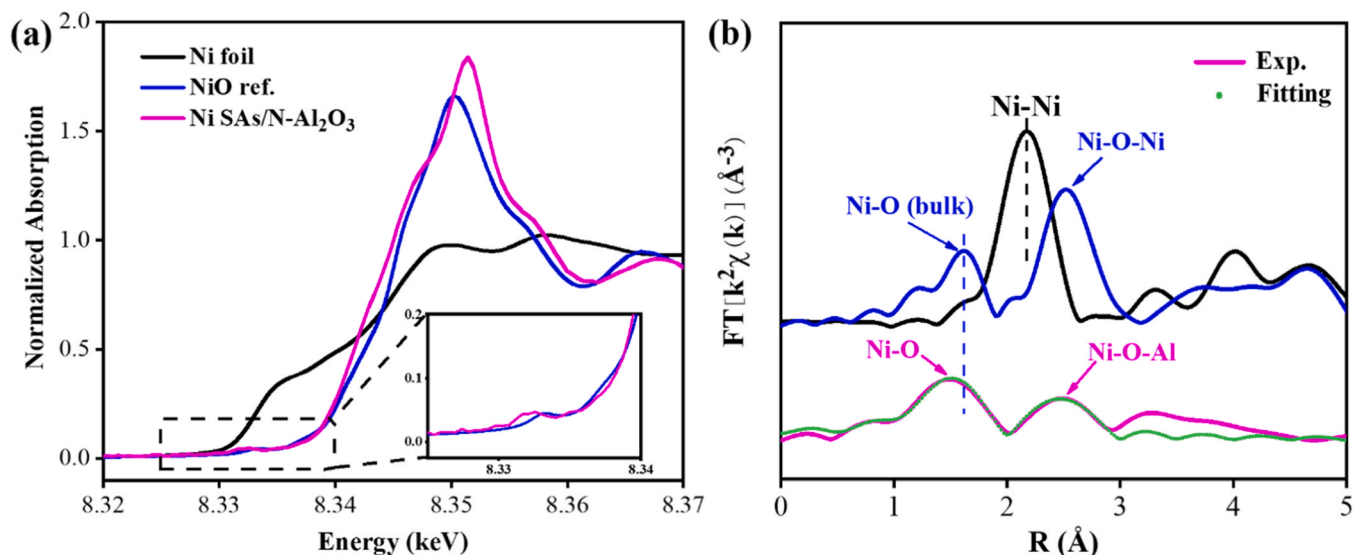
Fig. 3. (a) Ni K-edge XANES of Ni SAs/N-Al₂O₃ after treating at 600 °C under diluted H₂ flow for 1 h, and of Ni metal foil and NiO as references. The inset is an enlarged spectra of the region encased by the dashed rectangle. (b) Ni K-edge Fourier transformed EXAFS and corresponding fitting curve in the R space for Ni SAs/N-Al₂O₃ catalyst in comparison to Ni metal foil and NiO reference.
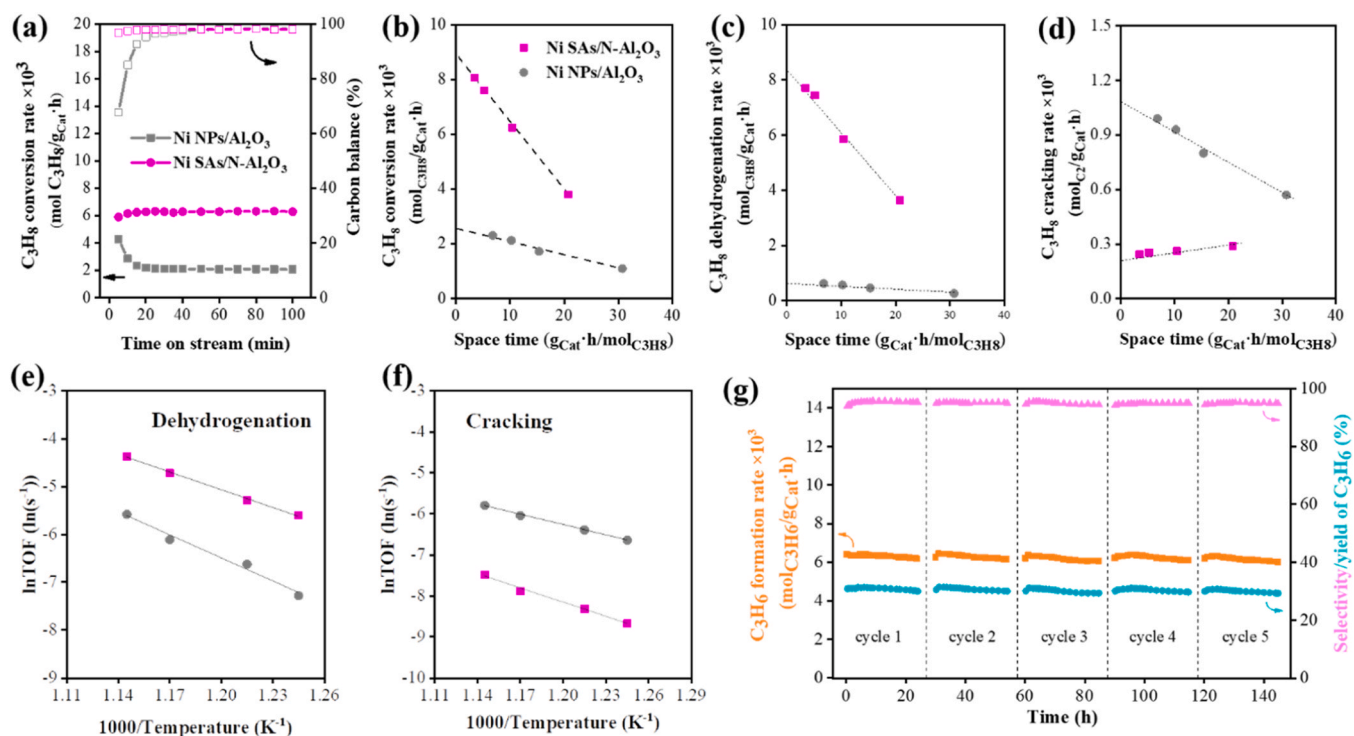

Fig. 4. (a) C₃H₈ conversion rates and carbon balance as a function of time on stream over alumina-supported Ni catalysts. Reaction conditions: T = 580 °C and 10.5 g_Cat·h/mol_C3H8 of space time. (b-d) Rates of C₃H₈ conversion, dehydrogenation, and cracking as a function of space time, respectively. Dotted lines indicate linear extrapolations to zero space time. (e, f) the Arrhenius plots of C₃H₈ dehydrogenation and cracking over alumina-supported Ni catalysts. Experimental conditions: T = 520–600 °C, 20 mL/min of C₃H₈/N₂. (g) Long-term stability test over Ni SAs/N-Al₂O₃ catalyst in five reaction-regeneration cycles.

previous studies [34], the high initial activity of Ni NPs catalyst has been attributed to the low-coordinated Ni atoms on the surface of Ni NPs. The rapid deactivation of Ni NPs catalyst within 10 min seems to be the result of the poisoning of such sites, according to previous studies [54, 55], which is also evidenced by the simultaneously incomplete carbon balance (~60%). Thus, the rate measurement for the Ni NPs/Al₂O₃ catalyst reported here was performed at steady state after the initial deactivation period.

Under the differential C₃H₈ conversions (3–10% C₃H₈) employed during reactivity measurements, there is a linear correlation between the C₃H₈ consumption/product yield and the catalyst loading at 580 °C (Fig. S16), suggests the PDH rates were measured in the kinetics regime. To eliminate the effect of secondary reactions on the kinetics measurements, the values of rate are determined by extrapolating to zero space time. Fig. 4b-d show C₃H₈ conversion, dehydrogenation, and cracking rates per g_Cat over the Ni SAs/N-Al₂O₃ and Ni NPs/Al₂O₃ catalysts,
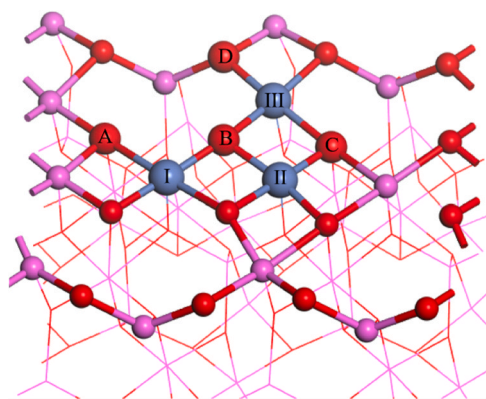
Fig. 5. Top view of the γ-Al$_2$O$_3$ (100) surface confined Ni single atom model, I/II/III denote three different sites that Ni could replace Al atom to form Ni SAC, A/B/C/D denote oxygen atoms with different coordination environments. Blue, purple and red represent Ni, Al and O atoms, respectively.

respectively. As observed in Fig. 4b, the rates of C$_3$H$_8$ conversion over both alumina-supported Ni catalysts decrease with increasing space time, possibly due to the inhibition by the products of C$_3$H$_8$, H$_2$ for instance [56,57]. At zero space time, the C$_3$H$_8$ conversion rate is determined to be 8.9 mmol$_{C3H8}$·g$_{Cat}^{-1}$·h^{-1} on the sample of Ni SAs/-N-Al$_2$O$_3$, which is 3.5 times higher than that on the Ni NPs catalyst (2.5 mmol$_{C3H8}$·g$_{Cat}^{-1}$·h^{-1}). For Ni SAs/N-Al$_2$O$_3$, the carbon-based selectivity of C$_2$H$_4$ is close to twice that of CH$_4$, suggesting the stoichiometry of C$_3$H$_8$ cracking into C$_2$H$_4$ and CH$_4$, as shown in Fig. S16c-d. Thus, the rates of C$_3$H$_8$ dehydrogenation and cracking can be calculated based on the mole selectivity toward C$_3$H$_6$ and C$_2$H$_4$, respectively. The higher rate of C$_3$H$_8$ dehydrogenation on Ni SAs/N-Al$_2$O$_3$ than Ni NPs/Al$_2$O$_3$, by a factor of 12 (8.6 vs 0.7 mmol$_{C3H8}$·g$_{Cat}^{-1}$·h^{-1}) is notable in Fig. 4c. Correspondingly, the Ni NPs/Al$_2$O$_3$ catalyst shows a higher rate of C$_3$H$_8$ cracking, suggesting that the lattice-embedded Ni atoms favor the dehydrogenation pathway while Ni NPs promote the cracking of C$_3$H$_8$.

The large difference between the PDH rates on different nickel sites is also confirmed by activation energy measurements. Apparent activation energies (*E*a) for C$_3$H$_8$ dehydrogenation and cracking were determined by plotting ln(TOF) versus 1/T in the temperature range of 520–600 °C. The metal dispersion of Ni NPs/Al$_2$O$_3$ is calculated based on the average size of Ni NPs, giving a Ni dispersion of 28%. For C$_3$H$_8$ dehydrogenation, the experimentally measured *E*a on Ni SAs/N-Al$_2$O$_3$ catalyst is 102.6 kJ/mol, which is much lower than that on the Ni NPs/Al$_2$O$_3$ catalyst (133.5 kJ/mol). On Ni SAs/N-Al$_2$O$_3$, a higher activation energy for cracking (139.7 kJ/mol) than for dehydrogenation leads to higher selectivity to C$_3$H$_6$, which is consistent with our PDH test results. The differences of *E*a for C$_3$H$_8$ dehydrogenation and cracking on these two sites further support that both dehydrogenation and cracking of C$_3$H$_8$ are catalyzed by the sites of Ni NPs, while the inhibition of C-C scission is promoted on sites of lattice-embedded Ni atoms.

Fig. 4g shows the result of the cycle stability test on the sample of Ni SAs/N-Al$_2$O$_3$. In the first cycle, an initial C$_3$H$_6$ formation rate of 6.4 mmol$_{C3H8}$·g$_{Cat}^{-1}$·h^{-1} accompanied by ~95% C$_3$H$_6$ selectivity is achieved, and the rate of C$_3$H$_6$ formation is only slightly decreased after 24 h of continuous operation (6.2 mmol$_{C3H8}$·g$_{Cat}^{-1}$·h^{-1}). The value of deactivation rate (k_d) is calculated to be 1.6×10^{-3} h^{-1} in the first PDH run. TG analysis of spent Ni SAs/N-Al$_2$O$_3$ sample after first PDH run gives ~3.6 wt% coke accumulations, as shown in Fig. S17, corresponding to about 1.6×10^{-3} g$_{coke}$/g$_{C3H6}$ on average, illustrating the coke inhibition capacity of Ni SAs/N-Al$_2$O$_3$ catalyst. Notably, the high C$_3$H$_6$ formation rate with a low k_d over Ni SAs/N-Al$_2$O$_3$ catalyst is comparable to reported state-of-the-art SACs for PDH, as listed in Table S3. In addition, the high yields of C$_3$H$_6$ (~30%) and low values of k_d (1.0–1.4 $\times 10^{-3}$ h^{-1}) are well maintained after five cycles, suggesting that the lattice-embedded Ni atoms are resilient under frequent reaction-

regeneration cycles at high temperatures.

3.3. DFT Calculations

The characterizations and PDH performance results of alumina-supported Ni catalysts indicate that tetrahedrally-coordinated Ni sites are active and highly selective towards the formation of C$_3$H$_6$. DFT calculations were further performed using the VASP software to corroborate the experimental results. For the (100) surface of γ-Al$_2$O$_3$, three different Al sites (I, II and III in Fig. 5) could be replaced by Ni atoms to generate the single atom sites Ni$_I$, Ni$_{II}$ and Ni$_{III}$. The site of Ni$_{II}$ is the most stable structure after optimization, and the energy of Ni$_I$ and Ni$_{III}$ is 0.46 eV and 0.64 eV higher than that of Ni$_{II}$ respectively. Many previous studies proposed that the first C-H bond activation is the key step for alkane activation. Generally, the first C-H bond cleavage can be divided into *CH$_x$ species binding to one surface site and *H species binding to adjacent site [58,59]. For example, Xie et al. [60] reported that C$_3$H$_8$ can be activated at coordinatively unsaturated Al-O pairs on Al$_2$O$_3$, leading to the formation of Al-CH$_2$CH$_2$CH$_3$ and O-H species. In this study, there are four different adjacent O sites (A/B/C/D) on the γ-Al$_2$O$_3$ (100) surface (Fig. 5). The activation of propane first C-H bond of the secondary carbon by six different Ni-O ion pairs were calculated and the activation barriers are shown in Table S4. The Ni$_I$-O$_B$ site was found to have the strongest ability to activate the first C-H bond of propane with the activation barrier of 2.06 eV.

The entire reaction pathway of propane transfer to propylene on the site of Ni$_I$ is shown in Fig. 6. TS1 is the transition state for the propane secondary carbon C-H bond activation on the Ni$_I$-O$_B$ site with a free energy barrier of 2.06 eV. The bond lengths of activated hydrogen with the Ni$_I$, O$_B$, and propane secondary C are 1.78, 1.33 and 1.38 Å, respectively, which indicate that the Ni$_I$-O$_B$ ion pairs play a synergistic effect for C-H bond activation. The first step for propane primary carbon C-H bond activation on Ni$_I$-O$_B$ site was also calculated for comparison, the activation energy is 2.32 eV, which is 0.26 eV higher than that of the secondary carbon C-H bond activation, as shown in Fig. S18. After the first activation step, the intermediate Int1 with CH(CH$_3$)$_2$ adsorbed on the Ni$_I$ atom and H adsorbed on the O$_B$ site is formed. This structure is not very stable and endergonic (0.89 eV) compared with Int, see structures in Fig. 6. There are three possible reaction paths from int1. One path is the primary carbon C-H bond activation and form a propylene molecule. The barrier of this step is only 0.89 eV (TS2 in Fig. 6) and a propylene molecule adsorbed on Ni$_I$ is formed (Int2) with an exergonic 0.1 eV compared with Int1. The other two paths are secondary carbon C-H continuing to activation and C-C bond cleavage from *CH(CH$_3$)$_2$ species, but the activation energies are 1.32 and 2.13 eV respectively (Fig. S19). Thus, the *CH(CH$_3$)$_2$ species is more likely transform to propylene from Int1. After that, the propylene desorbs to the gas phase with the barrier only 0.08 eV (Int2 to Int3 in Fig. 6). The propylene deep dehydrogenation from Int2 to form CH$_3$CCH$_2$ * and CH$_3$CHCH* were also considered, the barriers are 1.44 eV and 1.59 eV respectively (Fig. S20). The barrier of C-C bond cracking from Int2 is about 2.98 eV (Fig. S20), which is much larger than propylene desorption energy barrier. These calculations are consistent with the experiment results that the single atom Ni site can transform propane to propylene with high selectivity. The two OH groups are around the Ni atom after the propylene desorbs to the gas phase (Int3 and Int4), resulting in little change of free energy. In order to regenerate the original Ni$_I$-O$_B$ active center, hydrogen from one OH group transfers to the Ni atom with barrier of 0.24 eV (TS3). Then hydrogen from Ni site and from O site combine together to generate a H$_2$ molecule with barrier of 0.93 eV.

Overall, this pathway undergoes two C-H bond activation and surface hydrogen combining, propane transformed to the propylene and H$_2$ endergonic with 0.14 eV at 853.15 K. The rate determining step is the first C-H activation with barrier of 2.06 eV, suggesting the feasibility of propane dissociation at high temperature. The high barriers for C-C cracking and deep dehydrogenation on single atom Ni site promote the
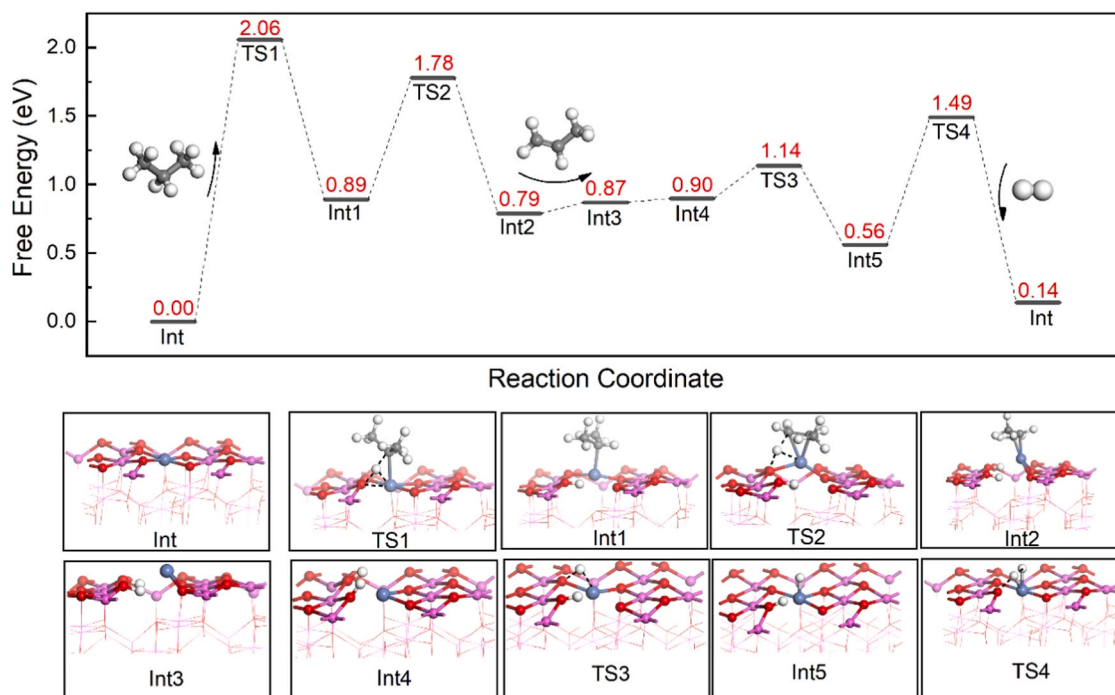
Fig. 6. Free-energy profiles at 853.15 K and 1 atm with the corresponding structures of intermediates and transition states for propane activation and transformation on Ni single atom catalyst, TS1 is the transition state of propane secondary carbon C-H bond activation on Ni_I-O_B ion pairs.

high selectivity to propylene for propane conversion.

4. Conclusions

In summary, we reported an efficient Ni-based single atom catalyst for improved propane dehydrogenation. The formation of lattice-embedded Ni SAC is demonstrated by combined characterizations, and the controllable synthesis of Ni-doped carbon dots is critical to achieve the substitution of Al cations by Ni atoms in the Al_2O_3 lattice and the formation of abundant channels on Al_2O_3 sheets. The resulting Ni SAC exhibits high activity and superior durability for the conversion of C_3H_8 toward C_3H_6. DFT results reveal that the active center of Ni-O ion pairs effectively activates C-H bonds while inhibiting further C-C cracking and secondary carbon C-H activation of surface-bonded $*CH(CH_3)_2$ species. Structural elucidation of the resulting Ni SAC by in situ XAS characterization suggests that the lattice-embedded Ni atoms in Al_2O_3 crystalline via $Ni-O_4$ coordination effectively avoids the reduction and aggregation of Ni^{2+} species, accounting for its excellent dehydrogenation stability under PDH reaction-regeneration cycles. This study on alumina lattice-embedded Ni SAC provides a general strategy for production of the thermally stable SACs for a wide range of high-temperature applications.

CRediT authorship contribution statement

Kou Jiajing: Funding acquisition, Project administration, Writing – original draft. **Gao Junxian:** Investigation, Writing – review & editing. **Ma Rui:** Conceptualization, Writing – original draft. **Dean David P:** Data curation, Formal analysis. **Zhou Bo:** Funding acquisition, Methodology, Writing – review & editing. **Zou Guojun:** Funding acquisition. **Miller Jeffrey T:** Funding acquisition, Software, Writing – review & editing. **Liang Kaijun:** Data curation. **Wang Junbo:** Data curation. **Wang Mingshan:** Data curation. **Liu Yuan:** Funding acquisition, Writing – original draft, Writing – review & editing.

Declaration of Competing Interest

The authors declare that they have no known competing financial interests or personal relationships that could have appeared to influence the work reported in this paper.

Data Availability

Data will be made available on request.

Supporting Information

Characterizations of Ni-CDs, alumina-supported Ni catalysts, DFT and catalytic results; characterizations include TEM, SEM, XRD, BET, EXAFS, and propane dehydrogenation reactions of the catalysts.

Appendix A. Supporting information

Supplementary data associated with this article can be found in the online version at doi:10.1016/j.apcatb.2024.123798.

References

[1] W. Jin, H. Shen, R. Qin, Q. Wu, K. Liu, N. Zheng, Surface and interface coordination chemistry learned from model heterogeneous metal nanocatalysts: from atomically dispersed catalysts to atomically precise clusters, Chem. Rev. 123 (2023) 5948–6002.

[2] M. Babucci, A. Guntida, B.C. Gates, Atomically dispersed metals on well-defined supports including zeolites and metal-organic frameworks: structure, bonding, reactivity, and catalysis, Chem. Rev. 120 (2020) 11956–11985.

[3] A. Wang, J. Li, T. Zhang, Heterogeneous single-atom catalysis, Nat. Rev. Chem. 2 (2018) 65–81.

[4] Y. Chen, S. Ji, C. Chen, Q. Peng, D. Wang, Y. Li, Single-atom catalysts: synthetic strategies and electrochemical applications, Joule 2 (2018) 1242–1264.

[5] J.J.H.B. Sattler, J. Ruiz-Martinez, E. Santillan-Jimenez, B.M. Weckhuysen, Catalytic dehydrogenation of light alkanes on metals and metal oxides, Chem. Rev. 114 (2014) 10613–10653.

[6] S. Chen, X. Chang, G. Sun, T. Zhang, Y. Xu, Y. Wang, J. Gong, Propane dehydrogenation: catalyst development, new chemistry, and emerging technologies, Chem. Soc. Rev. 50 (2021) 3315–3354.

[7] M. Huš, D. Kopač, B. Likozar, Kinetics of non-oxidative propane dehydrogenation on Cr_2O_3 and the nature of catalyst deactivation from first-principles simulations, J. Catal. 386 (2020) 126–138.

[8] W. Zhang, H. Wang, J. Jiang, Z. Sui, Y. Zhu, D. Chen, X. Zhou, Size dependence of Pt catalysts for propane dehydrogenation: from atomically dispersed to nanoparticles, ACS Catal. 10 (2020) 12932–12942.

[9] X. Chen, M. Peng, X. Cai, Y. Chen, Z. Jia, Y. Deng, B. Mei, Z. Jiang, D. Xiao, X. Wen, N. Wang, H. Liu, D. Ma, Regulating coordination number in atomically dispersed Pt species on defect-rich graphene for n-butane dehydrogenation reaction, Nat. Commun. 12 (2021) 2664.

[10] S. Ma, Z. Liu, Zeolite-confined subnanometric PtSn mimicking mortise-and-tenonjoinery for catalytic propane dehydrogenation, Nat. Commun. 13 (2022) 2716.

[11] J. Zhang, M. Wang, Z. Gao, X. Qin, Y. Xu, Z. Wang, W. Zhou, D. Ma, Importance of species heterogeneity in supported metal catalysts, J. Am. Chem. Soc. 144 (2022) 5108–5115.

[12] G.M. Whitesides, J.P. Mathias, C.T. Seto, Molecular self-assembly and nanochemistry: a chemical strategy for the synthesis of nanostructures, Science 254 (1991) 1312–1319.

[13] V.J. Cybulskis, B.C. Bukowski, H.-T. Tseng, J.R. Gallagher, Z. Wu, E.C. Wegener, A. J. Kropf, B. Ravel, F.H. Ribeiro, J. Greeley, J.T. Miller, Zinc promotion of platinum for catalytic light alkane dehydrogenation: insights into geometric and electronic effects, ACS Catal. 7 (2017) 4173–4181.

[14] Y. Nakaya, J. Hirayama, S. Yamazoe, K.-I. Shimizu, S. Furukawa, Single-atom Pt in intermetallics as an ultrastable and selective catalyst for propane dehydrogenation, Nat. Commun. 11 (2020) 2838.

[15] R.T. Hannagan, G. Giannakakis, R. Réocreux, J. Schumann, J. Finzel, Y. Wang, A. Michaelides, P. Deshlahra, P. Christopher, M. Flytzani-Stephanopoulos, M. Stamatakis, E. Sykes, First-principles design of a single-atom-alloy propane dehydrogenation catalyst, Science 372 (2021) 1444–1447.

[16] Y. Yuan, Z. Zhao, R.F. Lobo, B. Xu, Site diversity and mechanism of metal-exchanged zeolite catalyzed non-oxidative propane dehydrogenation, Adv. Sci. 10 (2023) 2207756.

[17] R. Lang, X. Du, Y. Huang, X. Jiang, Q. Zhang, Y. Guo, K. Liu, B. Qiao, A. Wang, T. Zhang, Single-atom catalysts based on the metal-oxide interaction, Chem. Rev. 120 (2020) 11986–12043.

[18] J. Shan, C. Ye, Y. Jiang, M. Jaroniec, Y. Zheng, S. Qiao, Metal-metal interactions in correlated single-atom catalysts, Sci. Adv. 8 (2022) 29.

[19] N. Daelman, M. Capdevila-Cortada, N. López, Dynamic charge and oxidation state of Pt/CeO_2 single-atom catalysts, Nat. Mater. 18 (2019) 1215–1221.

[20] L. Nie, D. Mei, H. Xiong, B. Peng, Z. Ren, X.I.P. Hernandez, A. Delariva, M. Wang, M.H. Engelhard, L. Kovarik, A.K. Datye, Y. Wang, Activation of surface lattice oxygen in single-atom Pt/CeO_2 for low-temperature CO oxidation, Science 358 (2017) 1419–1423.

[21] B. Qiao, A. Wang, X. Yang, L.F. Allard, Z. Jiang, Y. Cui, J. Liu, J. Li, T. Zhang, Single-atom catalysis of CO oxidation using Pt_1/FeO_x, Nat. Chem. 3 (2011) 634–641.

[22] S. Xie, L. Liu, Y. Lu, C. Wang, S. Cao, W. Diao, J. Deng, W. Tan, L. Ma, S.N. Ehrlich, Y. Li, Y. Zhang, K. Ye, H. Xin, M. Flytzani-Stephanopoulos, F. Liu, Pt atomic single-layer catalyst embedded in defect-enriched ceria for efficient CO oxidation, J. Am. Chem. Soc. 144 (2022) 21255–21266.

[23] W. Tan, S. Xie, Y. Cai, H. Yu, K. Ye, M. Wang, W. Diao, L. Ma, S. Ehrlich, F. Gao, L. Dong, F. Liu, Surface lattice-embedded Pt single-atom catalyst on ceria-zirconia with superior catalytic performance for propane oxidation, Environ., Sci. Technol. 57 (2023) 12501–12512.

[24] Z. Yang, H. Li, H. Zhou, L. Wang, L. Wang, Q. Zhu, J. Xiao, X. Meng, J. Chen, F. Xiao, Coking-resistant iron catalyst in ethane dehydrogenation achieved through siliceous zeolite modulation, J. Am. Chem. Soc. 142 (2020) 16429–16436.

[25] M.-M. Millet, G. Algara-Siller, S. Wrabetz, A. Mazheika, F. Girgsdies, D. Teschner, F. Seitz, A. Tarasov, S.V. Levchenko, R. Schlögl, E. Frei, Ni single atom catalysts for CO_2 activation, J. Am. Chem. Soc. 141 (2019) 2451–2461.

[26] Y. Dai, J. Gu, S. Tian, Y. Wu, J. Chen, F. Li, Y. Du, L. Peng, W. Ding, Y. Yang, $γ-Al_2O_3$ sheet-stabilized isolate Co^{2+} for catalytic propane dehydrogenation, J. Catal. 381 (2020) 482–492.

[27] Z. Hou, Y. Lu, Y. Liu, N. Liu, J. Hu, L. Wei, Z. Li, X. Tian, R. Gao, X. Yu, Y. Feng, L. Wu, J. Deng, D. Wang, M. Sui, H. Dai, Y. Li, A general dual-metal nanocrystal

[28] dissociation strategy to generate robust high-temperature-stable alumina-supported single-atom catalysts, J. Am. Chem. Soc. 145 (2023) 15869–15878.

[28] S. Ding, H.-A. Chen, O. Mekasuwandumrong, M.J. Hülsey, X. Fu, Q. He, J. Panpranot, C.-M. Yang, N. Yan, High-temperature flame spray pyrolysis induced stabilization of Pt single-atom catalysts, Appl. Catal. B: Environ. 281 (2021) 119471.

[29] M. Borrome, S. Gronert, Gas-phase dehydrogenation of alkanes: C–H activation by a graphene-supported nickel single-atom catalyst model, Angew. Chem., Int. Ed. 131 (2019) 15048–15052.

[30] D.E. Resasco, B.K. Marcus, C.S. Huang, V.A. Durante, Isobutane dehydrogenation over sulfided nickel catalysts, J. Catal. 146 (1994) 40–55.

[31] T. Saelee, S. Namuangruk, N. Kungwan, A. Junkaew, Theoretical insight into catalytic propane dehydrogenation on Ni(111), J. Phys. Chem. C. 122 (2018) 14678–14690.

[32] L. Xiao, P. Hu, Z. Sui, D. Chen, X. Zhou, W. Yuan, Y. Zhu, Rational design of intermetallic compound catalysts for propane dehydrogenation from a descriptor-based microkinetic analysis, J. Catal. 404 (2021) 32–45.

[33] G. Zhang, C. Yang, J.T. Miller, Tetrahedral nickel(II) phosphosilicate single-site selective propane dehydrogenation catalyst, ChemCatChem 10 (2018) 961–964.

[34] R. Ma, J. Gao, J. Kou, D.P. Dean, C.J. Breckner, K. Liang, B. Zhou, J.T. Miller, G. Zou, Insights into the nature of selective nickel sites on Ni/Al_2O_3 catalysts for propane dehydrogenation, ACS Catal. 12 (2022) 12607–12616.

[35] T. Ressler, WinXAS: A program for X-ray absorption spectroscopy data analysis under MS-Windows, J. Synchrotron Rad. 5 (1998) 118–122.

[36] J.J. Rehr, C.H. Booth, F. Bridges, S.I. Zabinsky, X-ray absorption fine structure in embedded atoms, Phys. Rev. B 49 (1994) 12347–12350.

[37] J.C. Serrano-Ruiz, A. Sepúlveda-Escribano, F. Rodríguez-Reinoso, Bimetallic PtSn/C catalysts promoted by ceria: application in the nonoxidative dehydrogenation of isobutene, J. Catal. 246 (2007) 158–165.

[38] F.T. Zangeneh, A. Taeb, K. Gholivand, S. Sahebdelfar, Kinetic study of propane dehydrogenation and catalyst deactivation over $Pt-Sn/Al_2O_3$ catalyst, J. Energy Chem. 22 (2013) 726–732.

[39] T. Lear, R. Marshall, J.A. Lopez-Sanchez, S.D. Jackson, T.M. Klapötke, M. Bäumer, G. Rupprechter, H.J. Freund, D. Lennon, The application of infrared spectroscopy to probe the surface morphology of alumina-supported palladium catalysts, J. Chem. Phys. 123 (2005) 174706.

[40] J.P. Perdew, K. Burke, M. Ernzerhof, Generalized gradient approximation made simple, Phys. Rev. Lett. 77 (1996) 3865–3868.

[41] G. Kresse, D. Joubert, From ultrasoft pseudopotentials to the projector augmented-wave method, Phys. Rev. B 59 (1999) 1758–1775.

[42] G. Kresse, J. Furthmüller, Efficiency of ab-initio total energy calculations for metals and semiconductors using a plane-wave basis set, Comp. Mater. Sci. 6 (1996) 15–50.

[43] G. Kresse, J. Furthmüller, Efficiency iterative schemes for ab initio total-energy calculations using a plane-wave basis set, Phys. Rev. B 54 (1996) 11169–11186.

[44] H.J. Monkhorst, J.D. Pack, Special points for Brillouin-zone integrations, Phys. Rev. B 13 (1976) 5188–5192.

[45] G. Henkelman, B.P. Uberuaga, H. Jónsson, A climbing image nudged elastic band method for finding saddle points and minimum energy paths, J. Chem. Phys. 113 (2000) 9901–9904.

[46] Q. Xu, R. Su, Y. Chen, S.T. Sreenivasan, N. Li, X. Zheng, J. Zhu, H. Pan, W. Li, C. Xu, Z. Xia, L. Dai, Metal charge transfer doped carbon dots with reversibly switchable, ultra-high quantum yield photoluminescence, ACS Appl. Nano Mater. 1 (2018) 1886–1893.

[47] G. Bharathi, D. Nataraj, S. Premkumar, M. Sowmiya, K. Senthilkumar, T. D. Thangadurai, O.Y. Khyzhun, M. Gupta, D. Phase, N. Patra, S. Nath Jha, D. Bhattacharyya, Graphene quantum dot solid sheets: strong blue-light-emitting & photocurrent-producing band-gap-opened nanostructures, Sci. Rep. 7 (2017) 10850.

[48] R.S. Sahu, A. Dubey, Y.-H. Shih, Novel metal-free in-plane functionalized graphitic carbon nitride with graphene quantum dots for effective photodegradation of 4-bromophenol, Carbon 182 (2021) 89–99.

[49] M. Nguefack, A.F. Popa, S. Rossignol, C. Kappenstein, Preparation of alumina through a sol-gel process. Synthesis, characterization, thermal evolution and model of intermediate boehmite, Phys. Chem. Chem. Phys. 5 (2023) 4279–4289.

[50] S.-M. Kim, Y.-J. Lee, J. Bae, H.S. Potdar, K.-W. Jun, Synthesis and characterization of a highly active alumina catalyst for methanol dehydration to dimethyl ether, Appl. Catal. A: Gen. 348 (2002) 113–120.

[51] A.A. Taromi, S. Kaliaguine, Synthesis of ordered mesoporous γ-alumina: effects of calcination conditions and polymeric template concentration, Micro Mesopor. Mater. 248 (2017) 179–191.

[52] P. Bai, P. Wu, Z. Yan, X. Zhao, A reverse cation-anion double hydrolysis approach to the synthesis of mesoporous $γ-Al_2O_3$ with a bimodal pore size distribution, Micro Mesopor. Mater. 118 (2009) 288–295.

[53] E. Groppo, C. Prestipino, F. Cesano, F. Bonino, S. Bordiga, C. Lamberti, P.C. Thüne, J.W. Niemantsverdriet, A. Zecchina, In situ, Cr K-edge XAS study on the Phillips catalyst: activation and ethylene polymerization, J. Catal. 230 (2005) 98–108.

[54] R.T. Vang, K. Honkala, S. Dahl, E.K. Vestergaard, J. Schnadt, E. Lægsgaard, B. S. Clausen, J.K. Nørskov, F. Besenbacher, Controlling the catalytic bond-breaking selectivity of Ni surfaces by step blocking, Nat. Mat. 4 (2005) 160–162.

[55] E. Nikolla, J.W. Schwank, S. Linic, Hydrocarbon steam reforming on Ni alloys at solid oxide fuel cell operating conditions, Catal. Today 136 (2008) 243–248.

[56] Y. Yuan, J.S. Lee, R.F. Lobo, Ga^+-chabazite zeolite: a highly selective catalyst for nonoxidative Propane dehydrogenation, J. Am. Chem. Soc. 144 (2022) 15079–15092.

[57] N.M. Phadke, E. Mansoor, M. Head-Gordon, A.T. Bell, Mechanism and kinetics of light alkane dehydrogenation and cracking over isolated Ga species in Ga/H-MFI, ACS Catal. 11 (2021) 2062–2075.

[58] R.T. Hannagan, G. Giannakakis, R. Réocreux, J. Schumann, J. Finzel, Y. Wang, A. Michaelides, P. Deshlahra, P. Christopher, M. Flytzani-Stephanopoulos, M. Stamatakis, E.C.H. Sykes, First-principles design of a single-atom-alloy propane dehydrogenation catalyst, Science 372 (2021) 1444–1447.

[59] K. Liang, X. Zeng, R. Ma, G. Zou, L. Dang, S. Li, A theoretical investigation of propane dehydrogenation on Pt and Ni-based alloys, J. Catal. 428 (2023) 115162.

[60] Z. Xie, Z. Li, P. Tang, Y. Song, Z. Zhao, L. Kong, X. Fan, X. Xiao, The effect of oxygen vacancies on the coordinatively unsaturated Al-O acid-base pairs for propane dehydrogenation, J. Catal. 397 (2021) 172–182.